ARCHIVES OF MECHANICS
Arch. Mech. **77** (5), 437–459, 2025, https://doi.org/10.24423/aom.4611

# Evaluating compression and nanoindentation in FCC nickel: a methodology for interatomic potential selection

K. CICHOCKI[1)], F. J. DOMINGUEZ-GUTIERREZ[2*)],
E. WYSZKOWSKA[2)], L. KURPASKA[2)], K. MUSZKA[1)]

[1)] *Faculty of Metals Engineering and Industrial Computer Science, AGH University of Krakow, Al. Mickiewicza 30, 30-059 Krakow, Poland*

[2)] *National Centre for Nuclear Research, NOMATEN CoE MAB+, Andrzeja Soltana 7, 05-400 Otwock-Swierk, Poland, e-mail*[*)]*: javier.dominguez@ncbj.gov.pl (corresponding author)*

We performed molecular dynamics simulations to investigate the mechanical response of face-centered cubic (FCC) nickel under uniaxial compression and nanoindentation using traditional interatomic potentials, including the embedded atom method (EAM) and the modified embedded atom method (MEAM). By calculating the generalized stacking fault energy (GSFE), we analyzed the dissociated slip paths responsible for stacking fault formation and partial Shockley dislocations during mechanical loading. Our findings highlight the critical importance of selecting appropriate interatomic potentials to model compression and nanoindentation tests accurately, aligning simulations with experimental observations. We propose a practical methodology for identifying empirical interatomic potentials suitable for mechanical testing of single-element materials. This approach establishes a benchmark for FCC nickel simulations and provides a basis for extending these methods to more complex Ni-based alloys, facilitating comparisons with experimental results such as those from electron microscopy.

**Key words:** mechanical test, MD simulations, nickel, nanoindentation, compression.



## 1. Introduction

Nickel is a well-known material with the FCC structure and is characterized by good mechanical properties like good toughness and ductility. Nickel also is a good conductor of heat and electricity [1], with superior corrosion resistance in caustic or nonoxidizing acidic solutions, and in gaseous halogens [2]. Because of the mentioned properties, nickel is used as an alloying element in stainless steels and in Ni-Cu, Ni-Cr-Fe [3] alloys, for example, to increase strength properties and corrosion resistance. In addition, due to their mechanical properties, over the years a number of nickel-based alloys have been

developed which are characterized not only by good corrosion resistance, but also by good creep resistance at high temperatures. Nickel-based alloys [4, 5] have found widespread use in industrial applications such as the aerospace industry [6] and in the nuclear power industry [7]. However, one must remember that this material activates under the neutron flux, so its high content should be avoided when considering internals that could suffer large neutron exposure. For this reason its content should be balanced in the FCC alloys and one way to do that is to optimize mechanical properties of the material by predicting their deformation behavior by MD simulations. Hence, usage of different available interatomic potentials should be considered at first.

Nanoindentation is a technique for measuring the mechanical properties of materials in small areas. The test involves inserting a suitable indenter of various geometries into the material in a direction perpendicular to its plane, with simultaneous measurement of the force versus displacement of the indenter. This method allows obtaining material parameters such as Young's modulus, hardness or even a yield point via analysis of the stress-strain curves [8, 9]. In the case of metals and alloys, the method makes it possible to determine mechanical properties and material parameters in the individual grain orientation. Nanoindentation simulations allow more accurate analysis of material behavior, and are used to characterize the material behavior when a force is applied. Simulations allow additional analysis of dislocation nucleation [9], the formation of stacking faults [10, 11] and the analysis of deformation mechanisms [12]. A number of publications show that MD simulations of nanoindentation allow a good analysis of the presented phenomena [13–20]. However, MD simulations are not without problems, one of the main ones being the selection of an appropriate potential for a given type of calculation [17–20].

In this work, we conducted molecular dynamics simulations to investigate the mechanical response of face-centered cubic (FCC) nickel under uniaxial compression and nanoindentation using traditional interatomic potentials, including the embedded atom method (EAM) and modified embedded atom method (MEAM) formulations. By calculating the generalized stacking fault energy (GSFE) for each potential, we analyzed the dissociated slip paths responsible for the stacking fault formation and the emergence of partial Shockley dislocations during mechanical loading. Our results emphasize the importance of establishing a benchmark for such simulations by identifying interatomic potentials capable of accurately modeling both compression and nanoindentation tests in a manner consistent with experimental observations. While machine learning-based interatomic potentials are increasingly popular due to their potential for improved accuracy, they often require robust training datasets and significant computational resources for large-scale simulations. In contrast, our study presents a practical methodology for selecting empirical interatomic potentials to perform mechan-

ical tests on single-element materials. This approach provides a foundation for comparison with electron microscopy observations and offers a pathway to extend the simulations to more complex Ni-based alloys.

## 2. Computational methods

To perform our simulations, we use the Large-scale Atomic/Molecular Massively Parallel Simulator (LAMMPS) [21] software which allows us to study the behavior of materials under a wide range of conditions. One of our goals is to accurately model plastic deformation, which is a crucial aspect of how materials respond to external loads. In this study, we employ traditional interatomic potentials based on the EAM and MEAM [22–26]. The selected potentials include EAM-1 by MALERBA *et al.* [22], which models Fe–Ni systems with stable ordered intermetallic phases L10-FeNi and L12-FeNi3, serving as a basis for simulating nickel's mechanical behavior. The EAM-2, developed by STOLLER *et al.* [23], focuses on modeling high-energy collision cascades in nickel, based on the density functional theory (DFT) calculations [24, 25], and effectively captures the mechanical response of irradiated nickel. The EAM-3 by ZHOU *et al.* [26] is used to model NiFe alloys, offering detailed information on dislocation dynamics under mechanical testing, which supports benchmarking for nickel-based tests. Additionally, we apply the MEAM potential by CHOI *et al.* [27], designed for the FCC Cantor alloy NiFeCrCoMn, which provides an accurate basis for simulating the nickel's mechanical response in complex alloy systems. We exclude recent machine learning-based interatomic potentials from our study due to their computational demands. Our focus on large-scale simulations with modest computational resources limits the feasibility of using these novel potentials, which often require access to supercomputers.

### 2.1. Sample preparation

We initially defined the FCC Ni sample with crystal orientations along [001], [101], and [111] by maintaining a density of approximately 8.78 g/cm$^3$. To achieve energy-optimized structures with an energy tolerance of $10^{-6}$ eV, we employed the FIRE (the fast inertial relaxation engine) 2.0 protocol, which effectively optimized the sample's energy and identified the lowest energy structure. Subsequently, the samples underwent a thermalization process at 300 K for 100 ps, utilizing the Nose–Hoover NPT thermostat with a time constant of 100 fs until the sample reaches a homogenous temperature and pressure profile [17–20]. To dissipate any artificial heat, a relaxation period of 10 ps was applied afterwards [19, 20].

### 2.2. Uniaxial compression test

MD simulations were performed for compression scenarios using a fully periodical numerical cell with dimension $(8.82, 9.88, 10.6)$ nm for [001], $(8.82, 6.99, 7.48)$ nm for [101], and $(6.25, 12.1, 18.3)$ nm for [111] with $8.4\times10^4$, $4.2\times10^4$, and $1.26\times10^5$ Ni atoms, respectively. Each sample is optimized and equilibrated to 300 K as explained before, MD simulations were then executed with a strain rate of $10^9$ s$^{-1}$ in the z-direction, where the atomic positions were remapped at each computational step to the instantaneous dimensions of the simulation cell [13, 20, 34]. This value for the strain rate is chosen due to the computational limitations inherent to MD simulations, which can only model systems on the scale of nanometers and nanoseconds. To observe meaningful deformation phenomena within these constraints, high strain rates are necessary to induce mechanical responses within the short simulation timescales. While this deviates from experimental conditions, the qualitative insights gained often remain valid, particularly for understanding mechanisms at the atomic scale. This approach ensured strict displacement-controlled straining of the cuboidal cell along the stretching direction, while a barostat was applied in the other two principal directions. The applied stress $\sigma_{zz}$ was directly obtained from the MD simulations by accounting for the number of atoms and their atomic volumes. The imposed uniaxial strain was calculated as $\varepsilon_{zz} = (L_z - L_{z0})/L_{z0}$, where $L_z$ is the instantaneous cell length along the straining $z$-axis, and $L_{z0}$ is the initial cell length prior to compression. A time step of 2 fs was used throughout the simulations [13].

### 2.3. Nanoindentation test

A numerical cell of $4.5\times10^6$, $4.48\times10^6$, and $4.7508\times10^6$ Ni atoms for the main crystal orientations [001] with a sample size of $(52.3, 52.3, 17.6)$ nm, [101] with a size of $(35.5, 34.35, 45)$ nm, and [111] with $(46.3, 46.3, 30)$ nm, respectively, are optimized and thermalized to 300 K. Before conducting the nanoindentation test, we divided the prepared sample into three sections along the z direction to establish appropriate boundary conditions. The two lowermost layers were kept frozen, covering approximately 0.02 times the size of the sample in the z-direction, which maintained the stability of the Ni atoms during the nanoindentation process. Additionally, a thermostatic region, located above the frozen layers, was included to effectively dissipate heat generated during the nanoindentation process. This thermostatic region has four times the thickness of the frozen section. The remaining layers constituted a region with dynamical atoms, where the interaction among atoms occurred as an indenter tip modified the surface structure and morphology. Furthermore, a 5 nm vacuum section was incorporated above the material sample [13–20]. In our simulation setup, we employed a non-atomic repulsive imaginary (RI) rigid sphere as an indenter tip, with a force potential

given by the equation $F(t) = K(r(t) - R)^2$. The force constant, $K = 236$ eV/A$^3$, denotes the specified force constant, ensuring high stiffness for our indenter tip and indenter tip radius $R = 12$ nm. The position of the indenter tip's center, denoted as $r(t)$, varied with time according to the equation $r(t) = (x_0, y_0, z_0 \pm vt)$. Here, $x_0$ and $y_0$ represented the center coordinates on the $xy$ plane of the surface sample, $z_0 = 0.5$ nm indicated the initial gap between the surface and the indenter tip, and the indenter tip moved at a speed of $v = 20$ m/s with a positive value for the loading process and negative for the unloading one [17–21]. The molecular dynamics (MD) simulations were conducted with periodic boundary conditions applied along the $x$ and $y$ axes to simulate an infinite surface. Each process was carried out for a duration of 225 ps, with a time step of $\Delta t = 1$ fs. The maximum duration of the simulation was determined by the desired duration of the loading stages. The load-displacement curve is then obtained by plotting the force on the indenter tip as a function of its displacement relative to the surface, as the indenter is driven into the material over time [13–20].

### 2.4. Experimental nanoindentation test

Nanoindentation tests of a Ni sample were carried out using a NanoTest Vantage system (Micro Materials Ltd) to characterize the mechanical properties. The system offers a force sensitivity of 3 nN and a depth sensitivity of 0.002 nm. The Synton-MDP diamond Berkovich indenter, with a tip radius typically ranging from 50 to 100 nm, was used for all measurements, making it well-suited for comparison with large-scale atomistic simulations in this study. The tests were performed under a 150 mN load, with 100 indentations spaced 100 μm apart on the sample.

## 3. Results

The GSFE is a valuable surrogate property for predicting the plastic response of a material, including its dislocation and twinning behavior. Thus, the variation of the system energy as a crystal undergoes translational slip along specific directions on a slip plane is known as the $\gamma$-surface. The maximum energy point on this surface, $\gamma_{usf}$, corresponds to the unstable stacking fault energy, which represents the energy barrier for dislocation nucleation at stress concentrations. A metastable point on the $\gamma$-surface, $\gamma_{sf}$, corresponds to the dislocation dissociation energy. To compute the GSFE, periodic boundary conditions were applied along the cut plane, using a replicated sample from a FCC unit cell with 13 957 Ni atoms and a dimension of $4.31 \times 2.59 \times 14.02$ nm$^3$. Displacements are applied in equal increments, each representing 0.1 of the Burgers vector magnitude. Following each displacement, the top and bottom atomic layers are fixed, while the

remaining layers relax exclusively in the $y$ direction. This relaxation process is performed using energy minimization with the conjugate gradient method and is considered complete when either (i) the ratio of the energy change between successive iterations to the most recent energy magnitude is less than $10^{-12}$, or (ii) the global force vector magnitude for all atoms is less than or equal to $10^{-12}$ eV/Å. Subsequently, the GSFE can be calculated as:

$$\gamma_{\mathrm{GSFE}} = \frac{E_s - E_0}{\mathrm{ASF}}, \tag{3.1}$$

where $E_s$ represents the energy of the sample at a given displacement, and $E_0$ denotes the energy for the perfect sample, ASF stands for the stacking fault area.

Figure 1 displays the computed GSFE for various displacement vectors, where atomic positions were relaxed only perpendicular to the cut plane showing the $\gamma$-lines along the $r/2$ in a) and $r/2$ in b) directions on the {111} plane (the most dense plane in FCC) determined from DFT [32, 33] and traditional interatomic potentials. Our results indicate that the MEAM potential overestimates the GSFE values for the $r$ slip system relative to DFT calculations [32, 33]. However, all the investigated potentials overestimate the GSFE for the $r$ direction compared to DFT [32, 33]. This discrepancy may explain the formation of unphysical defects observed in classical MD simulations to correctly simulate dislocation nucleation and dislocation dissociation behavior.

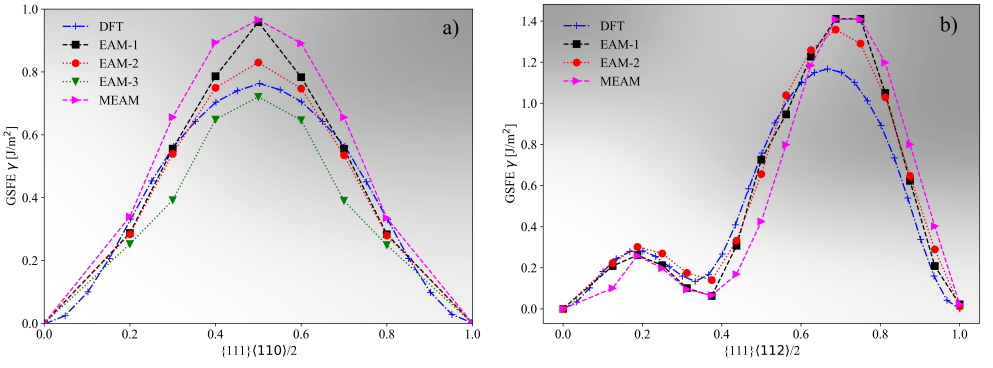


FIG. 1. Generalized Stacking Fault Energy (GSFE) surfaces for sl ip systems a) $r/2$ and b) $r/2$ on the {111} plane, calculated using DFT and various interatomic potentials. Atomic positions were relaxed perpendicular to the cut plane.

Shockley partial dislocations are separated by a stable stacking fault. Accurately modeling the dissociation of dislocations into partial dislocations and the subsequent separation of these partials is essential for precise modeling of plastic deformation mechanisms. In Fig. 2, we present results for the GSFE

for the $\gamma$-surface on the loosest packing {111} planes by different interatomic potentials. Our results indicate that the minimum energy path for the dissociation of full dislocations ($r/2$ or $r/2$) into Shockley partial dislocations on the {111} plane aligns with previously reported data [31]. However, the differences in energy values obtained from various computational approaches may lead to significant variations in the predicted behavior of dislocation nucleation and evolution. Specifically, these discrepancies could influence the likelihood of forming different dislocation types, such as Hirth or Frank dislocations, during external mechanical loading. Here, the MEAM potentials are recommended to model the nucleation of Shockely partials during mechanical testing.

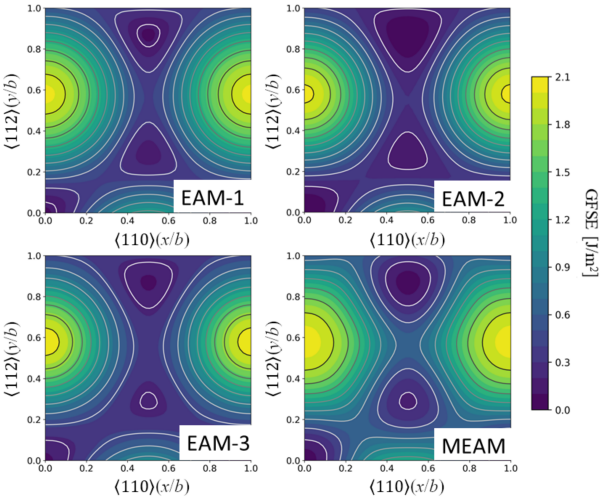


FIG. 2. GSFE for the $\gamma$-surface on the loosest packing {111} planes by different interatomic potentials showing the difference in modelling plastic deformation using different approaches.

To validate the suitability of the interatomic potentials for simulations under high-stress conditions, we evaluate the elastic constants over a pressure range relevant to the loading process [13, 14]. In the MD approach, the calculation of elastic constants $C_{ij}$ at zero temperature is based on analyzing the stress-strain response of a system. Initially, the material undergoes energy minimization to achieve equilibrium, ensuring the stress tensor accurately represents the system's relaxed state. Small, predefined strains are then incrementally applied to the simulation box, modifying its dimensions and, if necessary, its shape. For each strain increment, the components of the stress tensor are calculated. Pressure plays a crucial role in these calculations, as it directly influences the equilibrium state of the system. At zero pressure, the interatomic spacing and stress tensor are idealized for elastic constant computations, followed by increasing the pressure values during the optimization of the sample before the calculation of the elastic

constants $C_{ij}$. From the stress-strain relationship, the second derivatives of the strain energy are computed to obtain elastic constants, providing a detailed characterization of the material's mechanical response. This methodology ensures the calculated elastic constants reflect intrinsic material properties at the specified thermodynamic conditions. Additionally, we examine elastic stability by applying the spinodal, shear, and Born criteria under hydrostatic pressure $P$ [14]. These criteria, expressed as $M_1 = C_{11} + 2C_{12} + P > 0$, $M_2 = C_{44} - P > 0$, and $M_3 = C_{11} - C_{12} - 2P > 0$, are illustrated in Fig. 3. The materials demonstrate stability from 0 GPa to 50 GPa, which informs the setup of the numerical environment for nanoindentation simulations. However, for the EAM-2 potential, the Born criterion becomes negative beyond 40 GPa, rendering it unsuitable for high-pressure simulations.

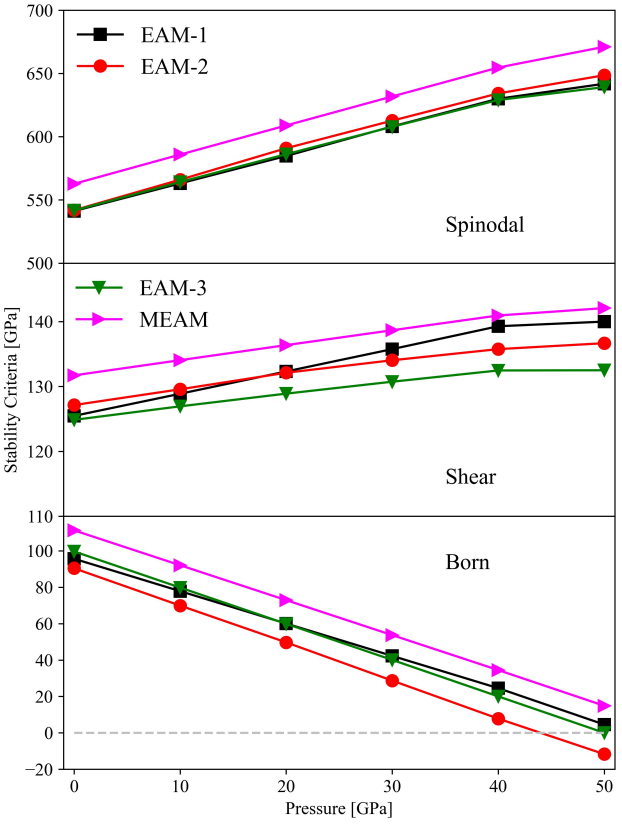


FIG. 3. Spinodal, shear, and Born stability criteria with hydrostatic pressure for different interatomic potentials. The pressure range showing the stability to set up the numerical conditions in the MD simulations.

### 3.1. Uniaxial compression test

In uniaxial compression simulations, we apply compressive strain along the $z$-axis using different interatomic potentials. This approach reduces the dimension along the compression axis while allowing the other dimensions to either remain constant. A controlled strain rate is applied, as higher strain rates can induce brittle behavior by limiting the time available for atomic rearrangements. In Fig. 4, we present the stress-strain responses for primary crystal orientations [001], [101], and [111] using several interatomic potentials. The results indicate that the mechanical response is similarly captured by the EAM-1 and EAM-3 potentials across different crystal orientations. In contrast, EAM-2 describes the elastic-to-plastic transition more gradually for the [001] orientation and aligns more closely with MEAM results for the [111] orientation, consistent

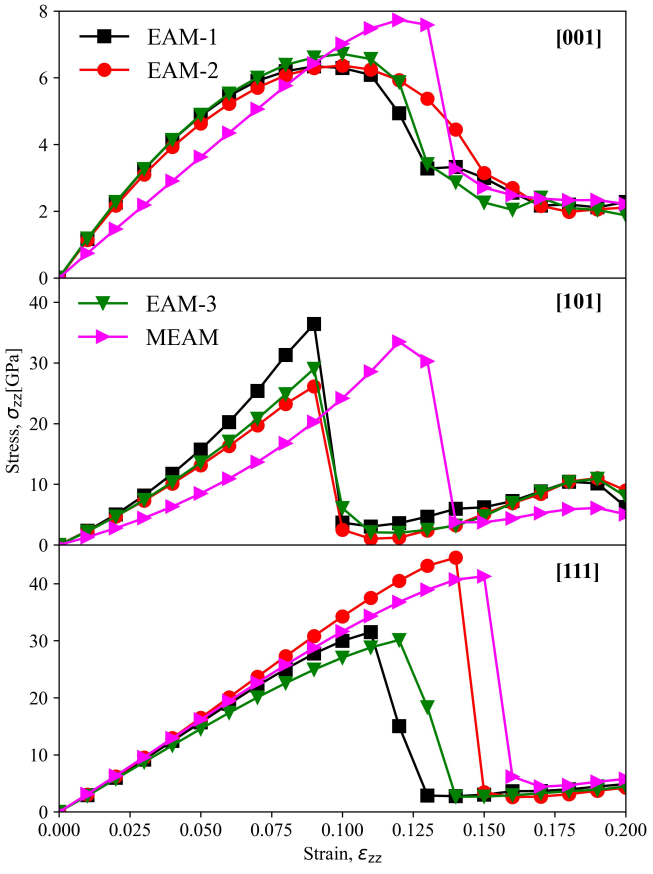


FIG. 4. Stress-strain curve for uniaxial compression simulations for the main crystal orientations [001], [101], and [111] by using different interatomic potentials.

with the GSFE profile. The MEAM potential captures a response more closely resembling typical experimental data for all crystal orientations, as it accounts for a more comprehensive description of nearest-neighbor interactions. Additionally, the ultimate stress is higher in simulations with the MEAM potential than with the EAM potentials, indicating that the initiation of plastic deformation requires greater strain with MEAM, which may better reflect experimental observations.

In Fig. 5, we present results for the dislocation length as a function of the strain for the [001] crystal orientation by different interatomic potentials. This analysis was performed using the Dislocation Extraction Algorithm (DXA) [30], which identifies and categorizes dislocation structures within atomistic microstructures. Dislocations were classified by their Burgers vectors into several types: $1/2\langle 110\rangle$ (perfect), $1/6\langle 112\rangle$ (Shockley), $1/6\langle 110\rangle$ (stair-rod), $1/3\langle 100\rangle$ (Hirth), and $1/3\langle 111\rangle$ (Frank). We observed that the nucleation of partial $1/6\langle 112\rangle$

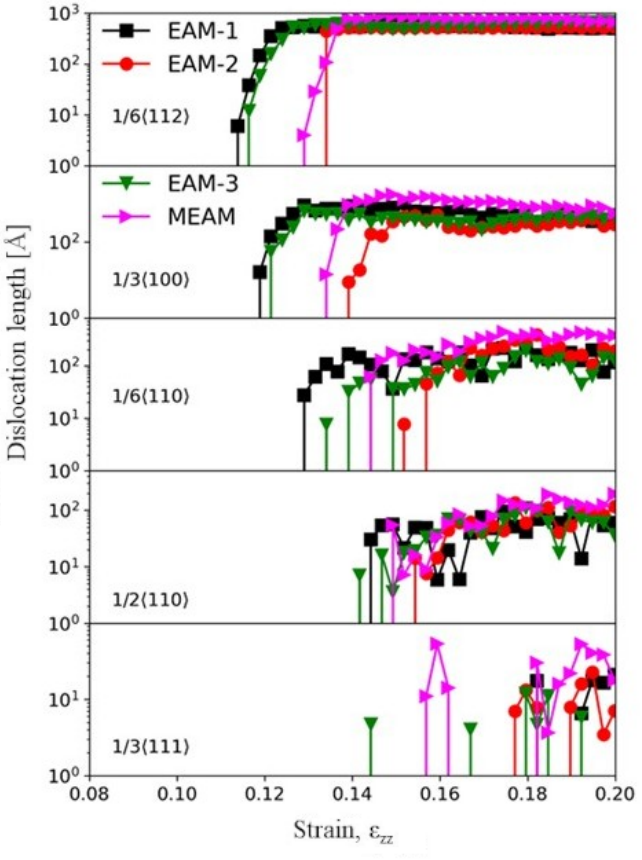


FIG. 5. Dislocation length as a function of the applied strain for [001] Ni by different interatomic potentials.

Shockley dislocations dominated during the uniaxial compression test at a strain of 0.12 and 0.14 with respect to the used interatomic potentials, which is characteristic of FCC structures. We also observed that different interatomic potentials model the nucleation of Frank dislocations in distinct ways, likely due to variations in their representation of Peierls–Nabarro energies. In contrast, the nucleation of Shockley and Hirth dislocations is modeled similarly across the different potentials, with only minor differences in the strain required to initiate plastic deformation.

In a compression test, the mechanical response of a material is largely governed by atomic-scale processes such as dislocation nucleation and stacking fault formation, and it can be observed at the initiation of the plastic deformation of the materials. At the onset of mechanical loading, the material shows an elastic deformation, with atomic rearranging, as observed in Fig. 4 for different crystal orientation and modeled in a similar way by the chosen interatomic potential. This stage produces a linear stress-strain relationship, and the material will revert to its original shape if the load is removed. As the applied stress increases and reaches the yield strength, plastic deformation begins. Dislocations start to nucleate, as shown in Fig 5. These initial dislocations allow for permanent deformation, as they can move and multiply under load. In FCC materials, partial dislocations move and can disrupt the atomic stacking sequence (e.g., ABCABC in FCC materials), leading to the formation of stacking faults. The ease of stacking fault formation depends on the material's SFE, as shown in Fig. 2; low-SFE materials favor wider stacking faults as partial dislocations separate more readily. These faults are often created by Shockley partial dislocations, which displace atoms in a way that results in intrinsic stacking faults. In FCC metals with a very low SFE, extensive stacking fault formation can even lead to twinning, where portions of the crystal form mirror-image atomic arrangements relative to the main lattice.

As compression deformation continues, dislocations multiply and interact with stacking faults, leading to increasingly complex behavior. Dislocation interactions can lead to obstacles such as dislocation pinning, cross-slip, or the formation of junctions, all of which contribute to strain hardening. This hardening effect arises because the growing density of dislocations and stacking faults makes it more difficult for new dislocations to move, thereby increasing the stress required for continued deformation. Eventually, the material reaches its yield point, beyond which local thinning, or necking, occurs. At this point, dislocation density is high, and interactions between dislocations and stacking faults may lead to local softening as dislocations start to rearrange or annihilate. Together, stacking faults and dislocations create a complex internal structure as shown in Fig. 6 for different interatomic potentials and at their corresponding strain value where the plastic deformation starts. We noticed that EAM-2 forms several SF more

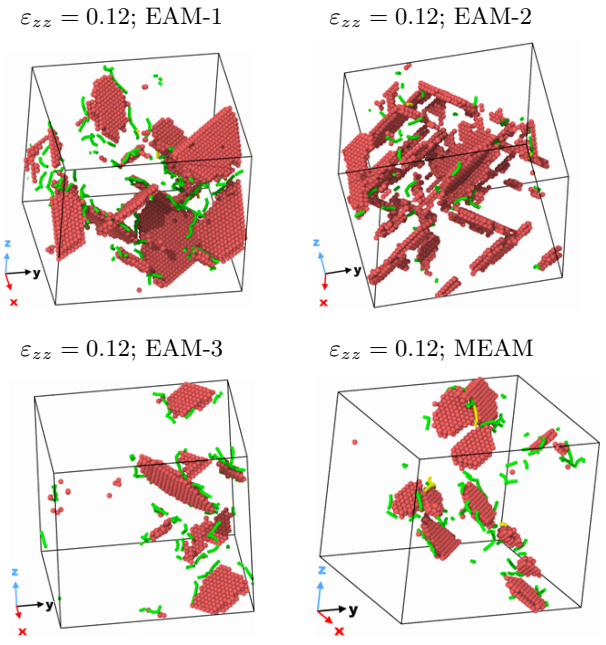


FIG. 6. Stacking fault formation and dislocation nucleation at the point of plastic deformation initiation for [001].

than the other potentials due to the GSFE energy information in the potential, while EAM-2 and MEAM model the mechanical response in a similar manner.

### 3.2. Nanoindentation test

During nanoindentation loading, the localized loading from the indenter tip initiates dislocation nucleation and multiplication at several stages during the loading, which are central to the material's plastic response. This mechanical response of the material can be analyzed from the load-displacement curves shown in Fig. 7 at different crystal orientations and by using different interatomic potentials. Initially, as the indenter makes contact with the surface, the material undergoes elastic deformation, where atomic bonds stretch but remain intact, allowing reversible displacement, where this elastic response can be fitted to the Hertz curve to compute the reduced elastic modulus [16–20]. As the indenter force increases, the stress beneath the tip exceeds the yield strength, triggering plastic deformation which is known as the pop-in event and identified as the deviation of the load curve with respect to the Hertz fitting curve [16, 20]. Sharp increases in displacement, known as pop-in events, can occur in the load-displacement curve; these are typically associated with the sudden nucleation and movement of many dislocations, resulting in an abrupt plastic deformation. Due

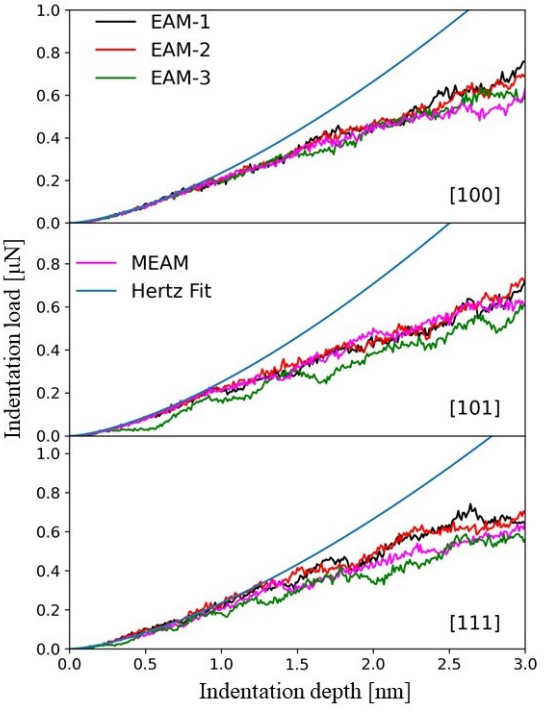


Fig. 7. Load displacement curves of nanoindentation loading at different crystal orientations and modeled by different interatomic potentials. The Hertz fitting curve is added to identify the elastic part of the process and the pop-in event.

to the high-stress concentration under the indenter, dislocations nucleate just beneath the surface. This process continues until the indenter tip is stopped. From our MD simulations, we observed the EAM potentials describe a similar mechanical response of the material under the external mechanical load for the [100] orientation, in agreement with MEAM results [16]. However, for [101] and [111] the EAM-3 results oscillate more due to the GSFE energy values. Nevertheless, all interatomic potentials model the elastic part of the nanoindentation loading process in good agreement, where the reduced Young modulus is the same value regardless of the chosen interatomic potential.

The Voigt–Reuss–Hill (VRH) approximation is a widely used method for estimating the effective elastic properties of materials based on their single-crystal elastic constants. It combines two theoretical bounds: the Voigt bound, which assumes uniform strain throughout the material, and the Reuss bound, which assumes uniform stress. The Voigt bound, representing a parallel distribution of crystals, provides an upper limit of the elastic modulus, while the Reuss bound, representing a series distribution of crystals, provides a lower limit. The VRH

approximation takes the arithmetic mean of these bounds, offering a realistic estimate of macroscopic elastic properties [32, 33]. This approach is particularly relevant for FCC metals due to their cubic symmetry and relatively low anisotropy, which make them well-suited for averaging methods. FCC metals are characterized by three independent single-crystal elastic constants, $C_{11}$, $C_{12}$, and $C_{44}$, which describe their response to normal and shear stresses. Using these constants, the bulk modulus is calculated from the Voigt and Reuss expressions as $K_{\mathrm{V}} = K_{\mathrm{R}} = \frac{1}{3}(C_{11} + 2C_{12})$, while the shear modulus is determined separately for each bound, with the Voigt approximation given by $G_{\mathrm{V}} = \frac{1}{5}(C_{11} - C_{12} + 3C_{44})$ and the Reuss approximation by $1/G_{\mathrm{R}} = \frac{5}{2}(1/(C_{11} - C_{12}) + 2/C_{44})$. The final shear modulus is obtained as the arithmetic mean $G_{\mathrm{VRH}} = (G_{\mathrm{V}} + G_{\mathrm{R}})/2)$, while the Young modulus and the Poisson ratio are derived from the bulk and shear moduli using standard isotropic elasticity relations. This methodology provides a robust framework for connecting the elastic properties of single crystals to the effective behavior of materials, making it particularly valuable for studying FCC metals and designing materials with tailored mechanical properties. Then, Young's modulus is calculated using the formula:

$$E_{\mathrm{VRH}} = \frac{9K_{\mathrm{VRH}}G_{\mathrm{VRH}}}{3K_{\mathrm{VRH}} + G_{\mathrm{VRH}}}, \tag{3.2}$$

where $K_{\mathrm{VRH}}$ and $G_{\mathrm{VRH}}$ are averaged bulk and shear moduli, respectively.

The NanoTest Vantage system produced by Micro Materials Ltd, has a software for data analysis which gives values such as the maximum depth and the plastic depth together with hardness and reduced modulus values. In a pyramidal indentation, the penetration depth of the calibrated indenter is measured as a function of the applied load during the load-unload cycle. During unloading the elastic component of the displacement starts to recover producing a sloped unloading curve. From this slope the elastic and plastic properties can be derived.

To obtain the elastic modulus from a nanoindentation test, the unloading portion of the load-displacement curve is analyzed according to a relation which depends on the contact area: $C = \pi^{0.5}/2E_rA^{0.5}$, where C is the contact compliance and $E_r$ is the reduced modulus defined by:

$$\frac{1}{E_r} = \frac{1 - v_s^2}{E_s} + \frac{1 - v_i^2}{E_i}, \tag{3.3}$$

where $v_s$ is Poisson's ratio for the sample, $v_i$ is Poisson's ratio for the indenter (0.07), $E_s$ is Young's modulus for the sample, and $E_i$ is Young's modulus for the indenter (1141 GPa) [35, 37]. In Table 1, we present a comparison between the VRH elastic modulus and the reduced elastic modulus to show the nanomechanical response of the material during the early stages of nanoindentation for each interatomic potential. The elastic constants at room temperature

Table 1. Comparison between reduced elastic constant in GPa obtained by nanoindentation test and by Voigt–Reuss–Hill approximation from the calculated $C_{ij}$ tensor, as well as experimental data for the [100] orientation from nanoindentation test and reported $C_{ij}$ values [40].

| $E_Y$ | EAM-1 | EAM-2 | EAM-3 | MEAM | Experiment |
|---|---|---|---|---|---|
| Reduced | 205.7 | 218.5 | 194.5 | 209.1 | 204 |
| VRH | 221.3 | 218.5 | 223.5 | 239.9 | 225.24 |

were calculated by combining the Born term, the stress fluctuation contribution, and the kinetic contribution [38, 39]. First, the Born term was obtained by applying small deformations to the relaxed structure and evaluating the resulting stress response, providing the static (0 K) elastic constants. Then, a MD simulation was performed at the target temperature to sample the stress tensor fluctuations. The thermal softening effect was accounted for by computing the stress-stress covariance matrix, while the kinetic contribution was evaluated using the equipartition theorem. The final elastic constants were obtained as $C = CB - Cs + Ct$, where $CB$ is the Born matrix, $Cs$ is the fluctuation correction, and $Ct$ is the kinetic term. This approach enables an accurate estimation of the elastic properties at finite temperature by including both anharmonic and kinetic effects beyond the static approximation. Experimentally, the VRH values were calculated using the reported elastic constants: $C_{11} = 253$ GPa, $C_{12} = 151$ GPa, $C_{44} = 124$ GPa [40]. We noticed that the EAM-1 and MEAM are the potentials that can describe the nanoindentation mechanisms properly for the FCC Ni single crystal regardless of the crystal orientations, reaching a good agreement with experimental values for the [100] Ni orientation.

In FCC Nickel, dislocations commonly nucleate as partial dislocations, in a similar way that in the compression simulation, each carrying a fraction of the full Burgers vector, which forms stacking faults and slip planes that help the material accommodate strain, as shown in Fig. 8 at the indentation depth of 3 nm. As the load increases, dislocations multiply and spread outwards, forming networks and allowing further plastic deformation such as the formation of prismatic dislocations loops. In principle, dislocation multiplication mechanisms, such as those involving Frank–Read sources [28], generate additional dislocations that propagate on slip planes, enabling the material to "flow" under the indenter, as observed in our MD simulations for indentation depths beyond the pop-in event [18–20]. As dislocations move, they encounter obstacles such as other dislocations, leading to pile-up, which in turn creates localized stress and contributes to work hardening [16, 20]. This work hardening requires a higher load to maintain further indentation. With continued loading, a plastic zone develops under the indenter, characterized by a high density of dislocations and the altered

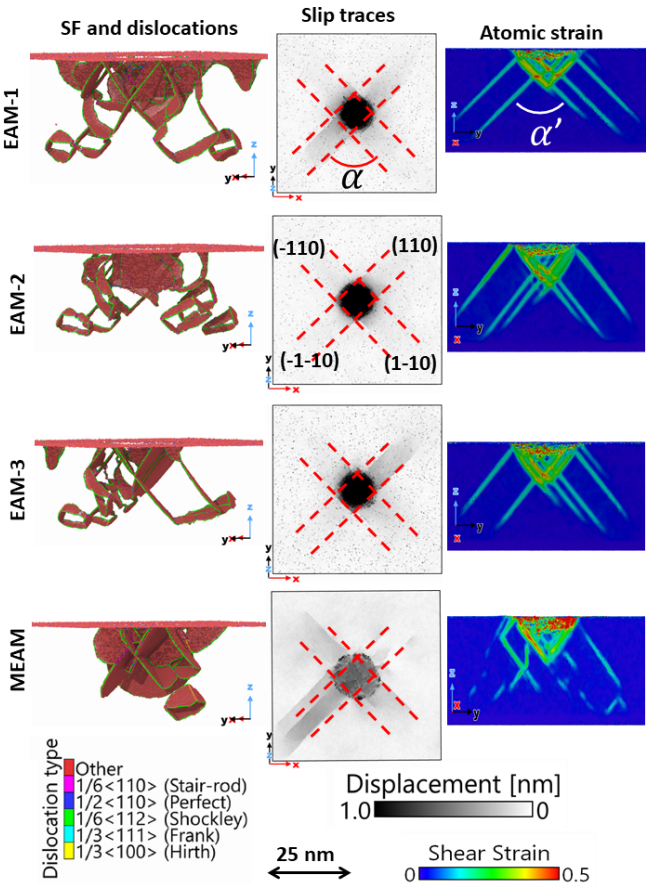


FIG. 8. Characterization of the indented Ni sample at [001] crystal orientation at an indentation depth of 3 nm. Identifying the SF, prismatic dislocation loops, slip traces on the [101] and symmetric planes (highlighted by dashed lines), and atomic strain mapping patterns by different interatomic potentials.

crystal structure, especially along slip planes in single crystals [16]. In Fig. 8, we present the visualization of the nanostructure of the indented samples at an indentation depth of 3 nm by characterizing the HCP atoms to visualize the formation of prismatic dislocation loops, as well as the dislocation associated with these defects. In addition, we calculate the displacements to visualize the slip traces formed during the mechanical load, and the strain for the Ni samples at the [001] orientations. Although the formation of slip traces on the surface and the strain patterns in the Ni samples are modeled in good agreement among the interatomic potentials, the formation and evolution of prismatic dislocation loops is modeled in different manner. While EAM-1 and EAM-2 results already nucleated 4 prismatic dislocation loops, EAM-3 has managed to create 2, which can be

attributed to the values of mechanical properties for each interatomic potential. Finally, MEAM is able to model the nucleation of these defects in more detail due to the surface information and description of the atoms at nearest neighbors.

Based on our simulations and the typical patterns of slip traces and strain mappings in FCC metals [16, 22], we observed that the angle, $\alpha$, characterizing the 4-fold rosette pattern of slip traces, varies across different crystal orientations and being independent of the chosen interatomic potential. Specifically, this angle is larger for the [111] orientation compared to that observed for the [100] orientation in Fig. 8, and it is smaller for the [011] orientation. Additionally, another angle, $\alpha'$, can be identified between the slip planes in the strain mapping. For the [011] orientation, $\alpha'$ is zero, indicating that loop propagation is parallel to the orientation planes, while for the [111] orientation, the angle $\alpha'$ is reduced. These findings highlight orientation-dependent differences in the slip behavior and strain distribution.

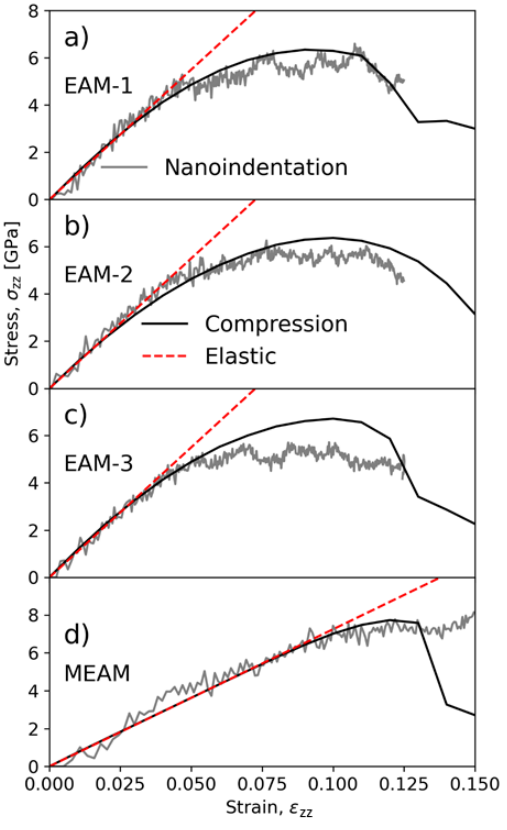


FIG. 9. Stress-strain curves for compression and nanoindentation simulations on the [001] Ni sample. We compare results for different interatomic potentials, noticing that MEAM is able to provide a good description of the plastic deformation of the material for both mechanical tests.

Nanoindentation and uniaxial compression can reveal different deformation mechanisms due to the difference in scale and the nature of loading. For example, during uniaxial compression, dislocation motion throughout the sample affects the response, while nanoindentation often initiates localized dislocations, stacking faults, or phase transformations, especially in the material beneath the indenter tip, as we have discussed. In Fig. 9, we present the stress-strain curves derived from uniaxial compression and nanoindentation simulations for the [001] orientation, following the protocol described in [12, 41]. An elastic reference curve, $\sigma_{zz} = E\varepsilon_{zz}$, is included to clearly delineate the elastic and elastic-plastic regions under load. Due to the inherently non-uniform strain field in nanoindentation, direct use of indentation strain without appropriate scaling would lead to inaccurate comparisons with uniaxial compression. To ensure a meaningful correlation, the strain values from nanoindentation simulations were rescaled to match those of compression simulations using a scaling factor: $\varepsilon_{zz}$ (compression) $= A\varepsilon_{zz}$ (nanoindentation), where $A$ was determined by aligning the elastic response of both loading conditions, ensuring consistency in the comparison of deformation behaviors. We observe good alignment between the two mechanical tests, particularly in the description of the elastic-to-plastic transition, where the computational models and interatomic potentials capture the material behavior effectively. This agreement between the two methods suggests that nanoindentation results can serve as a localized representation of bulk mechanical properties and that the selected modeling approach is robust for studying similar materials under varied loading conditions. The results obtained using EAM-1 and EAM-2 demonstrate that the deviation of the stress response from the linear elastic reference curve occurs at a similar strain value. In the plastic deformation regime, the nanoindentation stress follows the compression stress, with both approaches converging to the ultimate compression stress at the same strain, both EAM-1 performing in a better way. Similarly, the MEAM results exhibit strong agreement in the elastic region for both mechanical tests, where the stress-strain response deviates from linearity at the same strain value, and both nanoindentation and compression stress show consistent behavior for the transition from elastic to plastic deformation. However, the EAM-3 results indicate that the nanoindentation stress only partially follows the compression behavior in the plastic deformation region, suggesting a limitation in capturing post-yield deformation.

## 4. Concluding remarks

In summary, we have conducted molecular dynamics simulations to investigate the response of FCC Ni under uniaxial compression and nanoindentation using traditional interatomic potentials, highlighting the limitations and strengths of EAM- and MEAM-based approaches. For each potential, we calculated the

generalized stacking fault energy (GSFE) to examine the dissociated slip paths responsible for stacking fault formation and partial Shockley dislocations during mechanical loading. Our compression simulations reveal that EAM potentials tend to describe the material's plastic deformation after the yield point, though some EAM potentials have been modified to approximate dislocation formation, they generally lack details in this area. In contrast, MEAM potentials offer a more accurate description of both the elastic regime and the transition to plastic deformation, effectively modeling phenomena such as twinning and the formation of Shockley and Hirth dislocations, while requiring more computational resources. Similar trends were observed in nanoindentation simulations: load-displacement curves showed no notable differences between EAM and MEAM results, the nucleation of prismatic dislocation loops and the development of the dislocation network beneath the indenter tip were better captured by the MEAM potential. This indicates that MEAM provides a more reliable model for both uniaxial compression and nanoindentation in pure FCC Ni, as it accurately captures the transition from elastic to plastic deformation in both mechanical tests.

The selection of an appropriate empirical interatomic potential is essential for accurately modeling the mechanical response of FCC Ni, particularly in nanoindentation and tensile deformation simulations. The performance of EAM and MEAM potentials was evaluated based on their ability to reproduce key physical quantities governing dislocation-mediated plasticity and surface-driven deformation processes:

- **Generalized stacking fault energy (GSFE):** the potential must accurately capture the $\gamma$-surface, ensuring consistency with DFT calculations. A reliable GSFE profile is critical for describing the nucleation and evolution of stacking faults, which are primary deformation carriers in FCC metals under mechanical loading.
- **Surface energy and nanoindentation behavior:** the potential must yield accurate surface energy values, as deviations can significantly affect contact mechanics and stress localization during nanoindentation. The surface energy also influences the defect formation at free surfaces, impacting the material response under indentation loading.
- **Elastic response under pressure:** the pressure dependence of elastic constants must be correctly reproduced to prevent unphysical phase transformations. This ensures the structural stability of the FCC phase under high-stress conditions, maintaining mechanical fidelity across loading regimes.

By satisfying these criteria, the selected EAM and MEAM potentials provide a physically grounded and computationally efficient framework for modeling the mechanical behavior of FCC Ni. Their fidelity in capturing fundamental

defect energetics and elastic properties establishes their reliability for large-scale atomistic simulations of deformation processes. Consequently, our study presents a practical methodology for selecting empirical interatomic potentials to perform mechanical tests by MD simulations, our results indicate that while NiFe alloys can be effectively modeled by both EAM-1 [21] and MEAM [24] potentials modeling properly FCC Ni samples, more complex alloys are likely best represented by MEAM. The outcomes of this study establish a benchmark for pure FCC Ni and provide a foundation for extending simulations to more complex systems.

## Acknowledgments

Research was funded through the European Union Horizon 2020 research and innovation program under Grant Agreement No. 857470 and from the European Regional Development Fund under the program of the Foundation for Polish Science International Research Agenda PLUS, Grant No. MAB PLUS/2018/8, and the initiative of the Ministry of Science and Higher Education "Support for the activities of Centers of Excellence established in Poland under the Horizon 2020 program" under Agreement No. MEiN/2023/DIR/3795. We gratefully acknowledge Polish high-performance computing infrastructure PLGrid (HPC Center: ACK Cyfronet AGH) for providing computer facilities and support within computational Grant No. PLG/2024/017084. K.C. acknowledges support by Dean's grant 16.16.110.663 – task 13 AGH University of Krakow. The research project supported by the program "Excellence initiative – research university" for the AGH University of Krakow.

## References

1. F. Habashi, *Nickel, Physical and Chemical Properties*, [in:] R.H. Kretsinger, V.N. Uversky, E.A. Permyakov [eds.], Encyclopedia of Metalloproteins, Springer, New York, NY, 2013, https://doi.org/10.1007/978-1-4614-1533-6_338.

2. Z. Ahmad, *Chapter 9: Selection of materials for corrosive environment*, [in:] Z. Ahmad [ed.], Principles of Corrosion Engineering and Corrosion Control, Butterworth-Heinemann, 479–549, 2006, https://doi.org/10.1016/B978-075065924-6/50010-6.

3. J.H. Weber, *Nickel-based superalloys: Alloying*, [in:] K.H.J. Buschow, R.W. Cahn, M.C. Flemings, B. Ilschner, E.J. Kramer, S. Mahajan, P. Veyssière [eds.], Encyclopedia of Materials: Science and Technology, Elsevier, pp. 6146–6149, 2001, https://doi.org/10.1016/B0-08-043152-6/01090-1.

4. X. Liu, J. Fan, Y. Song, P. Zhang, F. Chen, R. Yuan, J. Wang, B. Tang, H. Kou, J. Li, *High-temperature tensile and creep behaviour of Inconel 625 superalloy sheet and its associated deformation-failure micromechanisms*, Materials Science and Engineering: A, **829**, 142152, 2022, https://doi.org/10.1016/j.msea.2021.142152.

5. T. BHUJANGRAO, F. VEIGA, A. SUÁREZ, E. IRIONDO, F.G. MATA, *High-temperature mechanical properties of IN718 alloy: comparison of additive manufactured and wrought samples*, Crystals, **10**, 689, 2020, https://doi.org/10.3390/cryst10080689.

6. I. DUL, *Application and processing of nickel alloys in the aviation industry*, Welding International, **27**, 1, 48–56, 2013, https://doi.org/10.1080/09507116.2011.600026.

7. D.Q. CHEN, G.-Y. ZHOU, Z.P. LIU, S.-T. TU, *Nanoindentation experimental study on mechanical properties of as-cast BNi-2 solder alloy*, Procedia Engineering, **130**, 652, 2015, https://doi.org/10.1016/j.proeng.2015.12.289.

8. R.A. MIRSHAMS, R.M. POTHAPRAGADA, *Correlation of nanoindentation measurements of nickel made using geometrically different indenter tips*, Acta Materialia, **54**, 1134, 2006, https://doi.org/10.1016/j.actamat.2005.10.048.

9. A.E. MAYER, V.S. KRASNIKOV, V.V. POGORELKO, *Homogeneous nucleation of dislocations in copper: Theory and approximate description based on molecular dynamics and artificial neural networks*, Computational Materials Science, **206**, 111266, 2022, https://doi.org/10.1016/j.commatsci.2022.111266.

10. A. JARLÖV, W. JI, Z. ZHU, Y. TIAN, R. BABICHEVA, R. AN, H.L. SEET, M.L.S. NAI, K. ZHOU, *Molecular dynamics study on the strengthening mechanisms of Cr–Fe–Co–Ni high-entropy alloys based on the generalized stacking fault energy*, Journal of Alloys and Compounds, **905**, 164137, 2022, https://doi.org/10.1016/j.jallcom.2022.164137.

11. Z. PAN, Y. FU, Y. WEI, X. YAN, H. LUO, X. LI, *Deformation mechanisms of TRIP–TWIP medium-entropy alloys via molecular dynamics simulations*, International Journal of Mechanical Sciences, **219**, 107098, 2022, https://doi.org/10.1016/j.ijmecsci.2022.107098.

12. F.J. DOMÍNGUEZ-GUTIÉRREZ, A. OLEJARZ, M. LANDEIRO DOS REIS, E. WYSZKOWSKA, D. KALITA, W.Y. HUO, I. JOZWIK, L. KURPASKA, S. PAPANIKOLAOU, M.J. ALAVA, K. MUSZKA, *Atomistic-level analysis of nanoindentation-induced plasticity in arc-melted NiFeCrCo alloys: The role of stacking faults*, Journal of Applied Physics, **135**, 185101, 2024, https://doi.org/10.1063/5.0200717.

13. F. DOMINGUEZ-GUTIERREZ, S. PAPANIKOLAOU, S. BONFANTI, M. ALAVA, *Plastic deformation mechanisms in BCC single crystals and equiatomic alloys: Insights from nanoindentation*, Computer Methods in Materials Science, **24**, 37–49, 2024, https://doi.org/10.7494/cmms.2024.1.0826.

14. J. REN, H. WU, L. WANG, Z. FAN, Y. QIU, L. YU, E. SHI, *Molecular dynamics simulation of nanoindentation of Nb–Zr alloys with different Zr content*, Metals, **12**, 1820, 2022, https://doi.org/10.3390/met12111820.

15. L. KURPASKA, F. DOMINGUEZ-GUTIERREZ, Y. ZHANG, K. MULEWSKA, H. BEI, W. WEBER, A. KOSINSKA, W. CHROMINSKI, I. JOZWIK, R. ALVAREZ-DONADO, S. PAPANIKOLAOU, J. JAGIELSKI, M. ALAVA, *Effects of Fe atoms on hardening of a nickel matrix: Nanoindentation experiments and atom-scale numerical modelling*, Materials and Design, **217**, 110639, 2022, https://doi.org/10.1016/j.matdes.2022.110639.

16. K. FRYDRYCH, F. DOMINGUEZ-GUTIERREZ, M. ALAVA, S. PAPANIKOLAOU, *Multiscale nanoindentation modelling of concentrated solid solutions: a continuum plasticity model*, Mechanics of Materials, **181**, 104644, 2023, https://doi.org/10.1016/j.mechmat.2023.104644.

17. A. NAGHDI, F.J. DOMÍNGUEZ-GUTIÉRREZ, W.Y. HUO, K. KARIMI, S. PAPANIKOLAOU, *Dynamic nanoindentation and short-range order in equiatomic nicocr medium-entropy alloy lead to novel density wave ordering*, Physical Review Letters, **132**, 116101, 2024, https://doi.org/10.1103/PhysRevLett.132.116101.

18. E. WYSZKOWSKA, C. MIESZCZYNSKI, Ł. KURPASKA, A. AZAROV, I. JÓŹWIK, A. KOSIŃSKA, W. CHROMIŃSKI, R. DIDUSZKO, W.Y. HUO, I. CIEŚLIK, J. JAGIELSKI, *Tuning heterogeneous ion-radiation damage by composition in $Ni_xFe_{1-x}$ binary single crystals*, Nanoscale, **15**, 4870–4881, 2023, https://doi.org/10.1039/D2NR06178C.

19. K. MULEWSKA, F.J. DOMINGUEZ-GUTIERREZ, D. KALITA, J. BYGGMÄSTAR, G.Y. WEI, *Self–ion irradiation of high purity iron: unveiling plasticity mechanisms through nanoindentation experiments and large-scale atomistic simulations*, Journal of Nuclear Materials, **586**, 154690, 2023, https://doi.org/10.1016/j.jnucmat.2023.154690.

20. F.J. DOMINGUEZ-GUTIERREZ, A. USTRZYCKA, Q.Q. XU, R. ALVAREZ-DONADO, S. PAPANIKOLAOU, M.J. ALAVA, *Dislocation nucleation mechanisms during nanoindentation of concentrated FeNiCr alloys: unveiling the effects of Cr through molecular simulations*, Modelling and Simulations in Material Science and Engineering, **30**, 085010, 2022.

21. A.P. THOMPSON, H.M. AKTULGA, R. BERGER, D.S. BOLINTINEANU, W.M. BROWN, P.S. CROZIER, P.J. IN'T VELD, A. KOHLMEYER, S.G. MOORE, T.D. NGUYEN, R. SHAN, M.J. STEVENS, J. TRANCHIDA, C. TROTT, S.J. PLIMPTON, *LAMMPS – a flexible simulation tool for particle-based materials modeling at the atomic, meso, and continuum scales*, Computer Physics Communications, **271**, 108171, 2022, https://doi.org/10.1016/j.cpc.2021.108171.

22. G. BONNY, R.C. PASIANOT, L. MALERBA, *Fe-Ni many-body potential for metallurgical applications*, Modelling and Simulation in Materials Science and Engineering, **17**, 025010, 2009, https://doi.org/10.1088/0965-0393/17/2/025010.

23. R.E. STOLLER, A. TAMM, L.K. BÉLAND, G.D. SAMOLYUK, G.M. STOCKS, A. CARO, L.V. SLIPCHENKO, Y.N. OSETSKY, A. AABLOO, M. KLINTENBERG, Y. WANG, *Impact of short-range forces on defect production from high-energy collisions*, Journal of Chemical Theory and Computation, **12**, 2871–2879, 2016, https://doi.org/10.1021/acs.jctc.5b01194.

24. P. HOHENBERG, W. KOHN, *Inhomogeneous electron gas*, Physical Review, **136**, B 864, 1964.

25. W. KOHN, L.J. SHAM, *Self-consistent equations including exchange and correlation effects*, Physical Review, **140**, A1133, 1965.

26. X.W. ZHOU, R.A. JOHNSON, H.N.G. WADLEY, *Misfit-energy-increasing dislocations in vapor-deposited CoFe/NiFe multilayers*, Physical Review B, **69**, 144113, 2024, https://doi.org/10.1103/physrevb.69.144113.

27. W.-M. CHOI, Y.H. JO, S.S. SOHN, S. LEE, B.-J. LEE, *Understanding the physical metallurgy of the CoCrFeMnNi high-entropy alloy: an atomistic simulation study*, npj Computational Materials **4**, 1, 2018, https://doi.org/10.1038/s41524-017-0060-9.

28. R.E. SMALLMAN, R.J. BISHOP, *Chapter 7 – Mechanical behaviour of materials*, [in:] R.E. Smallman, R.J. Bishop [eds.], Modern Physical Metallurgy and Materials Engineering, 6th ed., Butterworth-Heinemann, 197–258, 1999, https://doi.org/10.1016/B978-075064564-5/50007-0.

29. D.K. PATEL, S.R. KALIDINDI, *Correlation of spherical nanoindentation stress-strain curves to simple compression stress-strain curves for elastic-plastic isotropic materials using finite element models*, Acta Materialia, **112**, 295–302, 2016, https://doi.org/10.1016/j.actamat.2016.04.034

30. A. STUKOWSKI, *Visualization and analysis of atomistic simulation data with OVITO – the Open Visualization Tool*, Modelling and Simulation in Material Science and Engineering, **18**, 1, 015012, 2010.

31. X. GONG, Z. LI, A.S.L. SUBRAHMANYAM PATTAMATTA, T. WEN, D.J. SROLOWITZ, *An accurate and transferable machine learning interatomic potential for nickel*, Communications Materials, **5**, 157, 2024, https://doi.org/10.1038/s43246-024-00603-3.

32. Y. SU, S. XU, I.J. BEYERLEIN, *Density functional theory calculations of generalized stacking fault energy surfaces for eight face-centered cubic transition metals,* Journal of Applied Physics, **126**, 105112, 2019.

33. C.B. CARTER, C. HOLMES, *An accurate and transferable machine learning interatomic potential for nickel*, The Philosophical Magazine: The Journal of Theoretical Experimental and Applied Physics, **35**, 1161, 1977.

34. A. RIDA, M. MICOULAUT, E. ROUHAUD, A. MAKKE, *The effect of strain rate on the deformation processes of nc gold with small grain size*, Computational Materials Science, **172**, 109294, 2020.

35. D.H. CHUNG, W.R. BUESSEM, *The Voigt–Reuss–Hill (VRH) approximation and the elastic moduli of polycrystalline ZnO, TiO2 (Rutile), and α-Al2O3*, Journal of Applied Physics, **39**, 2777, 1968.

36. Y. LUO, *Isotropized Voigt-Reuss model for prediction of elastic properties of particulate composites*, Mechanics of Advanced Materials and Structures, **29**, 3934, 2021, https://doi.org/10.1080/15376494.2021.19137.

37. E. WYSZKOWSKA, C. MIESZCZYNSKI, Ł. KURPASKA, A. AZAROV, I. JÓŹWIK, A. KOSIŃSKA, W. CHROMIŃSKI, R. DIDUSZKO, W.Y. HUO, I. CIEŚLIK, J. JAGIELSKI, *Tuning heterogeneous ion-radiation damage by composition in $Ni_xFe_{1-x}$ binary single crystals*, Nanoscale, **10**, 4870, 2023, https://doi.org/10.1039/d2nr06178c.

38. K. VAN WORKUM, G. GAO, J.D. SCHALL, J.A. HARRISON, *Expressions for the stress and elasticity tensors for angle-dependent potentials*, Journal of Chemical Physics, **125**, 144506, 2006.

39. G. CLAVIER, N. DESBIENS, E. BOURASSEAU, V. LACHET, N. BRUSSELLE-DUPEND, B. ROUSSEAU, *Computation of elastic constants of solids using molecular simulation: comparison of constant volume and constant pressure ensemble methods*, Molecular Simulation, **43**, 1413, 2017, https://doi.org/10.1080/08927022.2017.1313418.

40. J.R. NEIGHBOURS, F.W. BRATTEN, C.S. SMITH, *The elastic constants of nickel*, Journal of Applied Physics, **23**, 389, 1952.

41. S. PATHAK, S.R. KALIDINDI, *Spherical nanoindentation stress-strain curves*, Materials Science and Engineering: R: Reports, **91**, 1–36, 2015, https://doi.org/10.1016/j.mser.2015.02.001.

*Received November 19, 2024; revised version April 26, 2025.*
*Published online July 11, 2025.*